

Where Are the Elements in Complex Aluminides? An Experimental and Theoretical Investigation of the Quasicrystalline Approximants, $\text{Mg}_{2-y}(\text{Zn}_x\text{Al}_{1-x})_{3+y}$

Chi-Shen Lee and Gordon J. Miller*

Contribution from the Department of Chemistry, Iowa State University, Ames, Iowa 50011-3111

Received October 21, 1999

Abstract: The first detailed investigation of the crystalline R-phases in the Mg–Zn–Al ternary system is reported, which will assist with the interpretation and understanding of similar quasicrystalline phases in this phase diagram. Although “ $\text{Mg}_{32}(\text{Zn},\text{Al})_{49}$ ” was originally reported by Bergman and Pauling in 1956, some details regarding its structure and the atomic arrangement remain to be solved. Single-phase product can be obtained from reaction compositions “ $\text{Mg}_{1.63}(\text{Zn}_x\text{Al}_{1-x})_{3.37}$ ”, $0.35 \leq x \leq 0.65$. A combination of single-crystal X-ray diffraction, powder neutron diffraction, energy dispersive spectroscopy, densities, and theoretical modeling is needed to elucidate a complete structural model for these phases. Single-crystal X-ray diffraction gave the R-phase structure (space group $Im\bar{3}$, $Z = 32$) for three difference samples: $\text{Mg}_{1.76(1)}\text{Zn}_{1.46(6)}\text{Al}_{1.65(3)}$ ($a = 14.364(3)$ Å), $\text{Mg}_{1.75(1)}\text{Zn}_{1.80(2)}\text{Al}_{1.31(1)}$ ($a = 14.212(1)$ Å), and $\text{Mg}_{1.73(1)}\text{Zn}_{2.46(6)}\text{Al}_{0.69(3)}$ ($a = 14.131(1)$ Å). Neutron powder diffraction on three similar bulk samples gave $\text{Mg}_{1.76(1)}\text{Zn}_{1.34(5)}\text{Al}_{1.76(5)}$ ($a = 14.2697(1)$ Å), $\text{Mg}_{1.75(1)}\text{Zn}_{1.76(5)}\text{Al}_{1.34(6)}$ ($a = 14.1804(1)$ Å), and $\text{Mg}_{1.73(1)}\text{Zn}_{2.06(3)}\text{Al}_{1.09(3)}$ ($a = 14.11247(6)$ Å). For all phases in this Mg–Zn–Al system, one crystallographic site (M4) has ca. 33% vacancies and shows a mixture of Mg and Zn atoms. Mg atoms occur next to vacancies on these sites. Theoretical calculations are used to explain the observed phase width involving Zn and Al, the trend in observed site occupancies, and the occurrence of vacancies in this structure. A range of nonbonding states near the Fermi level accounts for the phase width and allows a range in valence electron concentration between 2.07 and 2.48 for the existence of this structure. Valence electron concentrations in Mg–Zn–Al, however, necessitate the occupation of some metal–metal antibonding orbitals, which creates a driving force for vacancies. Since Mg can replace atoms in the (Zn,Al) framework, the R-phases are true intermediates between Zintl phases on one hand and Hume–Rothery intermetallic phases on the other.

Introduction

Intermetallic compounds provide a rich source of different structure types and special physical properties (electronic, magnetic, thermal, and mechanical) for potential applications as new functional materials (e.g., as permanent magnets or thermoelectric materials) as well as for studying the fundamental relationships among composition, structure, and properties.^{1–9} An important component of many intermetallics is aluminum due to its light atomic weight and conductivity properties, and it also deserves exceptional chemical interest. In the periodic table of elements, aluminum borders the transition from metallic to nonmetallic elements in the third period, while among the group 13 elements, it is the most electropositive.¹⁰ In

fact, the ground-state structure of each group 13 element differs from each of the others; the structure adopted by a given element is governed by the amount of valence s,p orbital mixing.^{11,12}

Aluminum combines with few other main group metals, viz., Li, Mg, Ca, Sr, and Ba, to form intermetallic compounds whose structures and properties follow simple valence rules. LiAl is a classic Zintl phase, with Al forming the diamond network.^{13,14} Other examples, like CaAl_2 ,^{15,16} CaAl_4 ,¹⁷ and $\text{Ba}_7\text{Al}_{13}$,^{2,18} show electronic structures similar to those of Zintl phases: there is a distinct minimum in the total electronic densities of states (DOSs) at the Fermi level, which is indicative of weakly conducting behavior. Orbitals at and below the Fermi level have bonding and nonbonding characteristics; those above the Fermi

(1) Westbrook, J. H.; Fleischer, R. L. *Intermetallic Compounds: Principles and Practice*; John Wiley & Sons: West Sussex, 1995; Vol. 1–2.

(2) Villars, P.; Calvert, L. D. *Pearson's Handbook of Crystallographic Data for Intermetallic Phases*, 2nd ed.; ASM International: Metals Park, OH, 1991.

(3) Nesper, R. *Angew. Chem.* **1991**, *103*, 805–834; *Angew. Chem., Int. Ed. Engl.* **1991**, *30* (7), 789–817.

(4) Miller, G. J. *Eur. J. Inorg. Chem.* **1998**, 523–536.

(5) Nesper, R. *Prog. Solid State Chem.* **1990**, *20*, 1–45.

(6) Belin, C.; Tillard-Charbonnel, M. *Coord. Chem. Rev.* **1998**, 178–180, 529–564.

(7) Schaefer, H. *Annu. Rev. Mater. Sci.* **1985**, *15*, 1–41.

(8) Belin, C.; Tillard-Charbonnel, M. *Prog. Solid State Chem.* **1993**, *22*, 59–109.

(9) Corbett, J. D. *Struct. Bonding (Berlin)* **1997**, *87*, 157–193.

(10) Huheey, J. E.; Keiter, E. A.; Keiter, R. L. *Inorganic Chemistry: Principles of Structure and Reactivity*, 4th ed.; Harper Collins College Publishers: New York, 1993.

(11) Häussermann, U.; Simak, S. I.; Abrikosov, I. A.; Sven, L. *Chem. Eur. J.* **1997**, *3*, 904.

(12) Häussermann, U.; Simak, S. I.; Ahuja, R.; Johansson, B.; Sven, L. *Angew. Chem., Int. Ed.* **1999**, *38*, 2017.

(13) Zintl, E. *Naturwissenschaften* **1929**, *17*, 782.

(14) Kishio, K.; Brittain, J. O. *J. Phys. Chem. Solids* **1979**, *40*, 933.

(15) Iandelli, A. *J. Less-Common Met.* **1987**, *135*, 195.

(16) Nesper, R.; Miller, G. J. *J. Alloys Compd.* **1993**, *197*, 109–21.

(17) Miller, G. J.; Li, F.; Franzen, H. F. *J. Am. Chem. Soc.* **1993**, *115*, 3739–3745.

(18) Fornasini, M. L.; Bruzzone, G. *J. Less-Common Met.* **1975**, *40*, 335.

level are antibonding.^{4,19} These intermetallics are usually brittle, diamagnetic, and weakly conducting.^{5,19,20} On the other hand, with group 11 or 12 elements, aluminum forms Hume–Rothery phases, which are typically soft metals with close-packed structures.²¹ For Hume–Rothery phases, chemical bonding properties are not readily discerned from the generally featureless DOS curves but instead require details of the energy band structure in reciprocal space.²² The structures within these two classes of intermetallic compounds follow simple electron-counting schemes based upon the average number of valence electrons per atom, called the valence electron concentration (VEC): (1) Hume–Rothery phases occur for total VEC less than or equal to two electrons per atom and (2) Zintl phases are valence compounds in which the VEC of the electronegative component exceeds four electrons per atom. A gap in our understanding of the relationships among VEC, structure, and properties exists between these two classes of intermetallic compounds.

As part of a research program to elucidate structural, electronic, and chemical bonding properties in complex aluminides and other intermetallics, our group is systematically investigating “hybrid” materials, $A_xT_yAl_z$, that involve components of both Zintl-type and Hume–Rothery-type phases (A is an alkaline earth or rare earth element; T is a late transition element).^{23–25} Experimental and theoretical results on A–Cu–Al, A–Au–Al, and A–Zn–Al systems indicate that compositions and structures lead to filled bonding and nonbonding orbitals of the $[T_yAl_z]$ framework, just as in Zintl phases, but with no energy gap in the total DOS.²³ The VECs of these aluminide substructures vary between two and four electrons per atom and allow a systematic study of the transition from Hume–Rothery-type to Zintl-type intermetallic compounds. Among the alkaline earth elements, magnesium represents a significant decrease in size and increase in electronegativity from calcium, strontium, or barium.¹⁰ Consequently, Mg can contribute to the network of strong orbital interactions and become more involved in the $[T_yAl_z]$ frameworks of ternary aluminides than its heavier analogues. This paper reports on a specific collection of substances in the Mg–Zn–Al system.

The title compounds were identified during a systematic investigation of the Mg–Zn–Al system with the reaction composition of $Mg_2(Zn_xAl_{1-x})_3$, $0 \leq x \leq 3$. Over 30 years ago, Bergman, Waugh, and Pauling reported the crystal structure of $Mg_{32}(Zn,Al)_{49}$, which is currently used as a model to discuss the atomic structure of quasicrystalline phases in the Mg–Zn–Al system.^{26,27} Accordingly, this phase belongs to a collection of crystalline intermetallic phases called “quasicrystalline approximants”, and the structure of $Mg_{32}(Zn,Al)_{49}$ is labeled the R-phase.^{28,29} Thermodynamic investigations of the Mg–Zn–

Al phase diagram indicate that the R-phase exists for a range of compositions close to $Mg_2(Zn_xAl_{1-x})_3$ and $Mg(Zn_xAl_{1-x})_2$ ($0.3 < x < 0.65$),³⁰ but no structural characterizations exist. The quasicrystalline phases of this system have been prepared at compositions close to $Mg_{32}(Zn_xAl_{1-x})_{49}$ using a rapid-quench method.^{31–34} However, a systematic study of the relationship among composition, crystal structure, chemical bonding, and physical properties of the crystalline phases has not been reported.

In this paper, we report the synthesis and detailed characterization of a series of crystalline R-phases in the Mg–Zn–Al system. The major goals of this work are (1) to determine the phase width of the R-phase structure and to establish its relationship to the total VEC of the substance; (2) to elucidate unequivocally the distribution of the elements in this structure, which is frequently cited to model quasicrystalline phases; (3) to evaluate the chemical bonding characteristics of these phases to establish a link between electronic structure and composition; and (4) to characterize the physical properties of these crystalline phases. The difficulty in differentiating Mg and Al in X-ray diffraction experiments necessitates neutron diffraction as an alternative method to assist in solving the site preference problem in these structures. However, since the elastic scattering factors for Mg and Zn are close to one another, a thorough structural chemical analysis of this system requires information from both techniques.

Experimental Section

Synthesis. All materials were handled in an Ar-filled glovebox (O_2 concentration < 10 ppm) and prepared from the elements. Starting materials were Mg turnings (Johnson-Matthey, 99.9%), Zn powder (Alfa, 99.9%), Al ingots (Alfa, 99.9999%), and Al foil. Reactions were carried out in sealed Ta ampules (Alfa, 99.99%; washed with 15% HF/35% HNO_3 /50% H_2SO_4 solution and dried) that were either sealed in fused silica tubes or placed in a fused silica Schlenk tube under reduced pressure. Reactant mixtures were heated to 1123 K for 24 h to ensure complete melting, followed by either quenching to room temperature or annealing at 768 K for 4 weeks. The title compounds were initially identified by X-ray powder diffraction patterns on products from target compositions of $Mg_2(Zn_xAl_{1-x})_3$ ($x = 0, 0.33, 0.67, 1.0$; VEC = 2.0–2.6³⁵). The binary systems ($x = 0$ and 1) showed mixtures of known elemental and binary phases, while the powder patterns of the $x = 0.33$ and 0.67 samples matched the theoretical pattern of $Mg_{32}(Zn,Al)_{49}$ with slightly different 2θ values to suggest a possible phase width for $Mg_{32}(Zn,Al)_{49}$. Crystals were selected from these two products for single-crystal X-ray diffraction and led us to investigate the phase width of the system $Mg_{2-y}(Zn_xAl_{1-x})_{3+y}$ in detail, based on the formula $Mg_{1.625}(Zn_xAl_{1-x})_{3.375}$ ($\equiv Mg_{52}(Zn_xAl_{1-x})_{108}$).

Eight reactions with different Zn:Al stoichiometric ratios in $Mg_{1.625}(Zn_xAl_{1-x})_{3.375}$ were carried out, and these results are summarized in Table 1. For each sample, the weighing error for each element is less than 0.5% by mass. The phases were identified by Guinier X-ray powder diffraction using an Enraf-Nonius Guinier camera with $Cu K\alpha_1$ radiation ($\lambda = 1.54056 \text{ \AA}$) and Si (NBS) as an internal standard. The products of every reaction were silvery, brittle ingots that were neither air nor moisture sensitive but decomposed readily in dilute acid (1.00

(19) Miller, G. J. In *Chemistry, Structure, and Bonding of Zintl Phases and Ions*; Kauzlarich, S. M., Ed.; VCH: New York, 1996; pp 1–59.

(20) Schaefer, H.; Eisenmann, B.; Mueller, W. *Angew. Chem.* **1973**, *85*, 742–760.

(21) Barrett, C. S.; Massalski, T. B. *Structure of Metals: Crystallographic Methods, Principles and Data*, 3rd ed.; Pergamon Press: Oxford, New York, 1980.

(22) Hume-Rothery, W. *The Metallic State*; Oxford: Clarendon, 1931; p 328.

(23) Nordell, K. J.; Miller, G. J. *Inorg. Chem.* **1999**, *38*, 579–590.

(24) Nordell, K. J.; Miller, G. J. *Angew. Chem., Int. Ed. Engl.* **1997**, *36*, 2008–2010.

(25) Nordell, K. J.; Miller, G. J. *Croat. Chem. Acta* **1995**, *68*, 825–835.

(26) Bergman, G.; Waugh, J. L. T.; Pauling, L. *Acta Crystallogr.* **1957**, *10*, 254.

(27) Bergman, G.; Waugh, J. L. T.; Pauling, L. *Nature* **1952**, *169*, 1057.

(28) Goldman, A. I.; Kelton, R. F. *Rev. Modern Phys.* **1993**, *65*, 213.

(29) Janot, C. *Quasicrystals: A Primer*, 2nd ed.; Oxford University Press: Oxford, 1994.

(30) Deshpande, N. U.; Ray, K. K.; Mallik, A. K. *J. Alloy Phase Diagrams* **1986**, *2*, 108.

(31) Baxter, D. V.; Richter, R.; Strom-Olsen, J. O. *Phys. Rev. B* **1987**, *35*, 4819.

(32) Shen, Y.; Shiflet, G. J. *Phys. Rev. B* **1988**, *38*, 5332.

(33) Cassada, W. A.; Shen, Y.; Poon, S. J.; Shiflet, G. J. *Phys. Rev. B* **1986**, *34*, 7413.

(34) Rajasekharan, T.; Akhtar, D.; Gopalan, R.; Muralidharan, K. *Nature* **1986**, *322*, 528.

(35) Note: the VEC value is calculated from the total number of valence electrons divided by the total number of atoms per formula unit. Mg is included because the electronegativity of Mg is similar to those of Al and Zn. The d electrons of Zn are not included.

Table 1. Summary of Reaction Compositions and Products Identified by Guinier X-ray Powder Diffraction and Single-Crystal X-ray Diffraction for Various Mg:Zn:Al Reactions

I. Guinier Powder X-ray			
reactions	x	identified phase ^a	mp (K) ^b
1. Mg ₂ (Zn _x Al _{1-x}) ₃			
Mg ₂ Al ₃	0.00	Mg ₂ Al ₃ + Al	722.2
Mg ₂ Zn ₂ Al	0.33	R-phase + Zn	790.5
Mg ₂ ZnAl ₂	0.67	R-phase + Al	780.8
Mg ₂ Zn ₃	1.00	MgZn ₂ + Al(tr)	na
2. Mg _{1.63} (Zn _x Al _{1-x}) _{3.37}			
Mg _{1.63} Al _{3.37}	0.00	Mg ₁₇ Al ₁₂ + unknown phase	723.8
Mg _{1.63} Zn _{0.64} Al _{2.73}	0.19	R-phase + Mg ₁₇ Al ₁₂	722.6
Mg _{1.63} Zn _{1.25} Al _{2.12}	0.37	R-phase + Al(tr)	na
Mg _{1.63} Zn _{1.42} Al _{1.95}	0.42	R-phase	780.1
Mg _{1.63} Zn _{1.72} Al _{1.65}	0.51	R-phase	763.2
Mg _{1.63} Zn _{2.16} Al _{1.21}	0.64	R-phase	765.5
Mg _{1.63} Zn _{2.76} Al _{0.61}	0.82	MgZn ₂ + Zn + R-phase	794.3
Mg _{1.63} Zn _{3.37}	1.00	MgZn ₂ + Zn	834.9
II. Single-Crystal Data			
reaction	x	crystal data	R1/wR2, %
3. Mg ₂ (Zn _x Al _{1-x}) ₃			
Mg ₂ Zn ₁ Al ₂	0.33	Mg _{1.76(1)} Zn _{1.46(3)} Al _{1.63(3)} (3) $a = 14.364(3)$ Å	6.64/3.03
Mg ₂ Zn ₂ Al ₁	0.67	Mg _{1.73(1)} Zn _{2.46(6)} Al _{0.69(3)} (1) $a = 14.131(1)$ Å	4.17/3.11
4. Mg _{1.63} (Zn _x Al _{1-x}) _{3.37}			
Mg _{1.63} Zn _{0.64} Al _{2.73}	0.19	Mg _{1.76(1)} Zn _{1.14(2)} Al _{1.97(2)} $a = 14.412(1)$ Å	2.11/4.01
Mg _{1.63} Zn _{1.42} Al _{1.95}	0.42	Mg _{1.76(1)} Zn _{1.76(1)} Al _{1.36(1)} $a = 14.297(1)$ Å	2.42/3.19
Mg _{1.63} Zn _{1.72} Al _{1.65}	0.51	Mg _{1.75(1)} Zn _{1.84(2)} Al _{1.31(1)} (2) $a = 14.212(3)$ Å	2.27/3.40
Mg _{1.63} Zn _{2.16} Al _{1.21}	0.64	Mg _{1.78(1)} Zn _{2.29(4)} Al _{0.81(4)} $a = 14.138(1)$ Å	2.34/3.72

^a All products were identified by Guinier Powder X-ray diffraction.

^b Only the melting point of the major phase is presented. ^c tr = trace amounts.

M HCl). According to X-ray photoelectron spectroscopy (XPS), Al₂O₃ and ZnO covered the surface of each product.

Since X-ray diffraction data and elemental analyses (discussed in the following paragraphs) could not provide a definitive picture of the Mg content and placement in the R-phases, three different compositions of Mg_{1.625}(Zn_xAl_{1-x})_{3.375} samples ($x = 0.63, 0.50, \text{ and } 0.37$) were prepared for neutron powder diffraction experiments. The previous reaction conditions were used, except that the final annealing procedure was changed to 768 K for 2 days. High, medium, and low Zn:Al molar ratios were chosen on the basis of reactions that could be prepared in nearly single phase.

Structural Characterization by X-ray Diffraction. Needle-shaped crystals for single-crystal X-ray diffraction experiments were selected from crushed products, mounted on glass fibers, and checked by means of rotation photographs and data collections on a Siemens P4 or a Rigaku AFC6R diffractometer using monochromatic Mo K α radiation. On these instruments, the intensities for every crystal were very weak for angles $2\theta > 40^\circ$ ($I/\sigma < 10$), and the ratios of unique reflections to independent parameters were low because the higher angle data were missed. These data are important because they are more sensitive to the chemical composition of a single crystal.

To improve the quality of the high-angle intensity data, a Bruker CCD-1000 diffractometer with monochromatic Mo K α radiation, $\lambda = 0.71073$ Å, and a detector-to-crystal distance of 5.08 cm was used for subsequent structural analyses at 298(2) K. For each crystal, data were collected in at least a quarter hemisphere and were harvested by collecting three sets of frames with 0.3° scans in ω for an exposure time of 30–60 s per frame. The ranges in 2θ values varied between 3.0° and values from 56.0° to 108.0° . The data were corrected for Lorentz and polarization effects. Absorption corrections were based

on fitting a function to the empirical transmission surface as sampled by multiple equivalent measurements.

The unit cell parameters were indexed by peaks obtained from 90 frames of reciprocal space images and then refined using all observed diffraction peaks after data integration. Systematic absences and Wilson plots³⁶ revealed a centrosymmetric, body-centered cubic crystal system with the Laue group $m\bar{3}$. Therefore, the space group $Im\bar{3}$ was chosen for subsequent structural analysis.

Structures of the R-phases were obtained by direct methods and refined by full-matrix least-squares refinement of F^2 using the SHELXTL 5.12 package.^{37–39} At least two individual single-crystal data sets were collected for each reaction to check the variation of the refined composition. Results of all single-crystal studies are available from the author. Table 2 summarizes the crystallographic data of three samples (**1**, **2**, and **3**) for which Guinier X-ray powder diffraction indicated that the R-phase is the only product. These samples represent the two extremes in Zn:Al ratios plus one intermediate composition. Table 3 gives atomic coordinates, site occupancies, and isotropic displacement parameters; Table 4 lists relevant internuclear distances.

Elemental Analysis. Energy dispersive spectroscopy (EDS) was performed on the same samples used for single-crystal X-ray diffraction experiments and on corresponding bulk samples using a Hitachi S-2460N scanning electron microscope. Internal standards of elemental Mg, Zn, and Al were included to determine the composition of each sample. At least four different points on each sample were measured to obtain the average chemical composition and standard deviations. Results for three different single-crystal and three different bulk samples are listed in Table 5.

Neutron Powder Diffraction. Micrometer-sized powders (less than 100 mesh) of “Mg_{1.625}Zn_{1.25}Al_{2.125}” (**4**), “Mg_{1.625}Zn_{1.688}Al_{1.688}” (**5**), and “Mg_{1.625}Zn_{2.125}Al_{1.25}” (**6**) were prepared for neutron diffraction studies as described above. The purity of each sample was checked by Guinier X-ray powder diffraction. Each sample was placed in a vanadium container and mounted on the general-purpose powder diffractometer (GPPD) at the Intense Pulsed Neutron Source (IPNS), Argonne National Laboratory.^{40,41} Time-of-flight neutron diffraction data were collected at 10(2) K and $2\theta = \pm 148.88^\circ$. The data were analyzed by Rietveld refinement with the GSAS software system.^{42–44} The lowest d spacing for all data was set at 0.8 Å.

The starting structural model of each sample came from the corresponding single-crystal X-ray diffraction study. Refined structural parameters included overall scale factors, lattice parameters, fractional coordinates, anisotropic thermal displacement parameters (only applied on Mg sites), and site occupancies. Absorption parameters and an extinction coefficient were also refined. Backgrounds were fit using a six-parameter analytical function, and peak shapes were fit using exponential pseudo-Voigt functions.⁴⁵ Contributions to the total pattern from impurity phases were also included in the refinement. The experimental and Rietveld refined profiles of these data are shown in Figure 1. Final compositions for each sample were ultimately set from a combination of elemental analyses, X-ray diffraction, and neutron diffraction refinements. Summaries of the crystallographic data and refinement, atomic positions, site occupancies and isotropic displacement parameters, and interatomic distances for each sample are listed

(36) Wilson, A. J. C. *Nature* **1942**, *150*, 151.

(37) S_AI_NT, Version 4; Siemens Analytical X-ray Instruments Inc.: Madison, WI, 1995.

(38) Sheldrick, G. M. *SHELXTL. Structure Determination Programs*, Version 5.12; Siemens Analytical X-ray Instruments Inc.: Madison, WI, 1995.

(39) Sheldrick, G. M. In *Crystallographic Computing 3*; Sheldrick, G. M., Kruger, C., Goddard, R., Eds.; Oxford University Press: Oxford, 1985; p 175.

(40) Von Dreele, R. B.; Jorgensen, J. D.; Windsor, C. G. *J. Appl. Crystallogr.* **1982**, *15*, 581.

(41) Jorgensen, J. D.; Rotella, F. J. *J. Appl. Crystallogr.* **1982**, *15*, 27.

(42) Rietveld, H. M. *J. Appl. Crystallogr.* **1969**, *2*, 65.

(43) Young, R. A. *The Rietveld Method*; Oxford University Press: Oxford, 1995.

(44) Larson, L. C.; Von Dreele, R. B. *Generalized Structural Analysis System (GSAS)*; LANSCE, MSH805; Los Alamos National Laboratory: Los Alamos, NM, 1995.

(45) Von Dreele, R. B. Unpublished work, 1990.

Table 2. Crystallographic Data for Three Samples of “Mg_{2-y}(Zn_xAl_{1-x})_{3+y}” from Single-Crystal X-ray Diffraction

reactions refined composition	Mg ₂ Zn ₂ Al ₁ Mg _{1.73(1)} Zn _{2.46(6)} Al _{0.69(3)} (1)	Mg _{1.64} Zn _{1.68} Al _{1.68} Mg _{1.75(1)} Zn _{1.80(2)} Al _{1.31(1)} (2)	Mg ₂ Zn ₁ Al ₂ Mg _{1.76(1)} Zn _{1.46(3)} Al _{1.65(3)} (3)
space group, <i>Z</i>	<i>Im</i> $\bar{3}$, 32	<i>Im</i> $\bar{3}$, 32	<i>Im</i> $\bar{3}$, 32
color of crystal	silver	silver	silver
temperature, K	298(2)	298(2)	163(2)
formula wt (g/mol)	7.08(6) × 10 ³	6.35(3) × 10 ³	5.82(5) × 10 ³
<i>a</i> (Å) ^a	14.131(1)	14.212(3)	14.364(3)
<i>V</i> (Å ³)	2822.0(4)	2871(1)	2963(1)
<i>d</i> _{calc} (g/cm ³)	4.17(4)	3.67(2)	3.26(3)
abs coeff (mm ⁻¹)	16.69	11.58	9.419
<i>F</i> (000)	3327.0	2950.4	2765
θ_{\min} , θ_{\max} (deg)	2.03, 28.93	2.03, 28.30	2.01, 28.23
reflections collected	9324	5450	6350
unique data (<i>I</i> ≥ 2σ(<i>I</i>))	777	681	675
radiation (Å)	0.710 73	0.710 73	0.710 73
refinement method		full-matrix least-squares on <i>F</i> ²	
<i>R</i> 1, <i>wR</i> 2 (all data) ^b	0.0417, 0.0311	0.0227, 0.0340	0.0664, 0.0303
goodness-of-fit on <i>F</i> ²	0.986	1.012	0.924
largest hole and peaks, e/Å ³	0.699 and -0.555	0.353 and -0.580	0.621 and -0.554

^a From Guinier powder patterns (room temperature). ^b *R*1 = ∑||*F*_o| - |*F*_c||/∑|*F*_o|; *wR*2 = [∑[*w*(*F*_o² - *F*_c²)²]/∑[*w*(*F*_o²)]^{1/2}, *w* = σ_{*F*}⁻².

Table 3. Atomic Positional Coordinates, Isotropic Displacement Parameters (Å²), and Site Occupancies for “Mg_{2-y}(Zn_xAl_{1-x})_{3+y}”

atom	site	<i>x</i>	<i>y</i>	<i>z</i>	<i>U</i> _{eq} ^a	site occ.
Mg _{1.73(1)} Zn _{2.46(6)} Al _{0.69(3)} (1)						
A1	12e	0.1991(1)	0	1/2	0.17(1)	Mg 1.000(1)
A2	16f	0.1862(1)	0.1862(1)	0.1862(1)	0.16(1)	Mg 1.000(1)
A3	24g	0	0.3005(1)	0.1167(1)	0.16(1)	Mg 1.000(1)
M1	24g	0	0.1795(1)	0.3074(1)	0.14(1)	Al 0.280(6) Zn 0.720(6)
M2	24g	0	0.929(1)	0.1514(1)	0.12(1)	Al 0.106(6) Zn 0.894(6)
M3	48h	0.1577(1)	0.1904(1)	0.4037(1)	0.15(1)	Al 0.268(5) Zn 0.732(5)
M4	12e	0.4032(1)	0	1/2	0.15(1)	Mg 0.27(2) Zn 0.40(1)
Mg _{1.75(1)} Zn _{1.80(2)} Al _{1.31(1)} (2)						
A1	12e	0.1970(1)	1/2	0	0.016(1)	Mg 1.000(1)
A2	16f	0.1860(1)	0.1860(1)	0.1860(1)	0.015(1)	Mg 1.000(1)
A3	24g	0.1163(1)	0.3007(1)	0	0.015(1)	Mg 1.000(1)
M1	24g	0.3063(1)	0.1788(1)	0	0.013(1)	Al 0.521(2) Zn 0.479(2)
M2	24g	0.1508(1)	0.926(1)	0	0.011(1)	Al 0.136(3) Zn 0.864(3)
M3	48h	0.3088(1)	0.3422(1)	0.968(1)	0.014(1)	Al 0.542(2) Zn 0.458(2)
M4	12e	0.4021(1)	1/2	0	0.015(1)	Mg 0.34(2) Zn 0.28(1)
Mg _{1.76(1)} Zn _{1.46(3)} Al _{1.65(3)} (3)						
A1	12e	0.1963(2)	0	1/2	0.010(1)	Mg 1.000(1)
A2	16f	0.1860(1)	0.1860(1)	0.1860(1)	0.010(1)	Mg 1.000(1)
A3	24g	0	0.3009(1)	0.1161(1)	0.011(1)	Mg 1.000(1)
M1	24g	0	0.1782(1)	0.3061(1)	0.010(1)	Al 0.672(5) Zn 0.328(5)
M2	24g	0	0.924(1)	0.1506(1)	0.009(1)	Al 0.159(5) Zn 0.841(5)
M3	48h	0.1578(1)	0.1915(1)	0.4034(1)	0.010(1)	Al 0.682(4) Zn 0.318(4)
M4	12e	0.4019(2)	0	1/2	0.010(1)	Mg 0.35(2) Zn 0.27(1)

^a *U*_{eq} is defined as one-third of the trace of the orthogonalized *U*_{*ij*} tensor.

in Tables 6–8. The refined compositions from neutron diffraction for each bulk product are also included in Table 5.

After the structure of the main phase was determined, refinements including impurities from the starting elements and possible binary phases were included. In addition to the three elements, an AuCu₃-type phase is present. The product of the “Mg_{1.625}Zn_{2.125}Al_{1.25}” reaction contains trace amounts of Al, while the other two samples contain trace amounts of Mg, Zn, Al, and an AuCu₃-type compound. The AuCu₃-

Table 4. Selected Interatomic Distances (Å) for Mg_{1.73(1)}Zn_{2.46(6)}Al_{0.69(3)} (1), Mg_{1.75(1)}Zn_{1.80(2)}Al_{1.31(1)} (2), and Mg_{1.76(1)}Zn_{1.46(3)}Al_{1.65(3)} (3)

		1	2	3
A1	A3 (2×)	3.059(1)	3.0754(9)	3.077(2)
	M1 (4×)	3.225(1)	3.2918(7)	3.311(2)
	M3 (4×)	3.050(1)	3.0927(7)	3.101(1)
	M3 (4×)	3.0797(5)	3.1162(4)	3.1227(7)
A2	M4	2.891(2)	2.933(2)	2.948(3)
	M4 (2×)	3.137(2)	3.147(1)	3.145(2)
	A2	3.133(3)	3.170(2)	3.178(4)
	A3 (3×)	3.248(1)	3.2806(6)	3.289(1)
A3	M1 (3×)	3.1491(5)	3.1698(4)	3.1750(6)
	M2 (3×)	2.991(1)	3.0196(9)	3.027(2)
	M3 (3×)	3.0935(8)	3.1150(6)	3.121(1)
	M3 (3×)	3.1089(9)	3.1339(6)	3.143(1)
M1	A3	3.306(3)	3.328(2)	3.329(3)
	M1	3.0351(8)	3.0517(6)	3.049(1)
	M1 (2×)	3.200(1)	3.228(1)	3.241(2)
	M2	2.981(1)	3.0170(9)	3.027(1)
M2	M2 (2×)	2.988(1)	3.0194(7)	3.028(2)
	M3 (2×)	3.111(1)	3.1376(8)	3.142(2)
	M3 (2×)	3.1235(8)	3.1597(5)	3.170(1)
	M4 (2×)	3.550(1)	3.5857(9)	3.590(2)
M3	M2	2.5286(7)	2.5418(5)	2.545(1)
	M3 (2×)	2.6225(5)	2.6551(4)	2.664(1)
	M3 (2×)	2.6793(6)	2.7170(5)	2.728(1)
	M4	2.9693(8)	3.0027(6)	3.007(1)
M4	M2	2.6330(9)	2.6487(6)	2.649(1)
	M2 (4×)	2.6491(6)	2.6651(4)	2.666(1)
	M3	2.7284(7)	2.7679(6)	2.6995(7)
	M3 (2×)	2.6767(4)	2.6928(4)	2.768(1)
M4	M4	2.9348(7)	2.9648(6)	2.970(1)
	M4	2.743(3)	2.801(2)	2.811(4)

type compound was indexed on the basis of six unidentified peaks (two independent and four overlapped peaks), and the composition was set at “MgZn”.

Physical Properties Measurements. (i) Density. Densities of single-phase products used for neutron diffraction and EDS investigations were measured pycnometrically in triplicate using 100 mesh powders and He as the displacement fluid on a multipycnometer (Quanta Chrome Corp.). The results are tabulated with the crystallographic data from powder neutron diffraction in Table 6.

(ii) Differential Thermal Analysis. Several powdered samples were used to perform differential thermal analysis (DTA) on a Perkin-Elmer DTA 7 running Pyris software version 3. The sample holder was purged with Ar for at least 30 min to remove oxygen and hydrogen before each measurement. Preliminary experiments indicated that all samples decomposed when the temperature was raised above 1023 K because

Table 5. Summary of Chemical Compositions for Single-Crystal and Bulk Materials from X-ray, Neutron, and EDS Experiments

no.		Mg	Zn	Al	d (g/cm ³)	VEC	remarks
Single Crystal							
1	X-ray	0.354(1)	0.504(1)	0.142(3)	4.17(4) ^a	2.14	2.2×10^{-2} mm ³
	EDS	0.350(6)	0.487(2)	0.163(3)		2.16	
2	X-ray	0.361(1)	0.370(2)	0.269(1)	3.67(2) ^a	2.28	4.4×10^{-3} mm ³
	EDS	0.346(5)	0.384(2)	0.270(3)		2.27	
3	X-ray	0.361(1)	0.300(3)	0.338(3)	3.26(3) ^a	2.32	1.3×10^{-2} mm ³
	EDS	0.397(5)	0.287(2)	0.316(3)		2.32	
Bulk Product							
4	neutron	0.35(2)	0.43(1)	0.22(1)	3.90(6) ^b	2.22	powder (<100 mesh)
	EDS	0.32(1)	0.48(1)	0.20(1)	4.10(3) ^c	2.20	
5	neutron	0.36(1)	0.36(1)	0.28(1)	3.62(9) ^b	2.28	powder (<100 mesh)
	EDS	0.34(1)	0.40(2)	0.26(2)	3.75(4) ^c	2.26	
6	neutron	0.36(1)	0.28(1)	0.36(1)	3.25(6) ^b	2.36	powder (<100 mesh)
	EDS	0.36(1)	0.30(2)	0.34(2)	3.4(1) ^c	2.34	

^a Calculated density from single-crystal X-ray data. ^b Calculated density from neutron diffraction data. ^c Pycnometer measurements.

elemental Zn vaporized. Each powder sample (ca. 30 mg) was heated from 473 to 973 K at a rate of 5 K/min and then cooled at the same rate to 473 K under Ar atmosphere. Guinier powder X-ray diffraction was performed before and after the DTA experiment on each sample. Table 1 lists some DTA results for each sample.

(iii) Magnetic Susceptibility Measurements. Temperature-dependent magnetic susceptibility measurements were conducted using a Quantum Design SQUID magnetometer operated at 3 T over the temperature range 6–300 K. Data were collected for the samples “Mg_{1.625}Zn_{1.375}Al_{2.00}”, “Mg_{1.625}Zn_{1.688}Al_{1.688}”, and “Mg_{1.625}Zn_{2.125}Al_{1.25}”. All three samples showed temperature-independent susceptibilities over the range 50–250 K. After corrections for the diamagnetic contributions of the constituent atomic cores and the sample holder,⁴⁶ all samples show Pauli paramagnetic behavior with average susceptibilities of $3.4(3) \times 10^{-3}$, $1.5(2) \times 10^{-3}$, and $3.0(2) \times 10^{-3}$ emu/mol, respectively.

(iv) Electrical Resistivity Measurements. A standard four-probe technique was used to measure the temperature-dependent resistivity for the “Mg_{1.625}Zn_{1.688}Al_{1.688}” sample from 1.8 to 300 K in fields of both 0 and 5.5 T. The irregular shape of the polycrystalline sample was first polished to form a metal plate and then cut into a rectangular bar by using a wire saw. The dimensions of the sample were $1 \times 1 \times 3$ mm³. Electrical contact was made to the sample using Epo-tek H2OE silver epoxy, with typical contact resistances of 1–2 Ω. The resistivity at 298(2) K is 62.47(1) μΩ·cm and decreases nearly linearly toward low temperatures, which is consistent with typical metallic behavior. At 5.5 T, the shape of the resistivity vs temperature curve did not change, but the resistivity measured at each temperature is 0.2–0.3 μΩ·cm higher than the zero field value (e.g., 62.67(6) μΩ·cm at 298-(2) K).

Electronic Structure Calculations. The electronic structures of various models of R-phases were calculated using the LCAO (tight-binding) approximation with the extended Hückel theory (EHT).^{47–50} Mg atomic orbital parameters were used for the three A sites (A1–A3), and Al atomic orbital parameters were used for the four M sites (M1–M4). Calculations using both Al and Zn atomic orbital parameters were also performed, but the results were essentially the same as those for calculations with just Al parameters. A primitive cell of 80 atoms (26 A and 54 M) was used for calculations of total and partial densities of states (DOSs), crystal orbital overlap population curves (COOPs), Mulliken populations, and Fermi energies.^{51,52} A special points set of

60 k points in the irreducible wedge of the first Brillouin zone was chosen to perform the integrations.⁵³ Atomic orbital parameters are as follows (all single-ζ STO functions): Mg, H_{ii}(3s) = −9.00 eV, H_{ii}-(3p) = −4.50 eV, ζ(3s) = ζ(3p) = 0.95; Al, H_{ii}(3s) = −12.3 eV, H_{ii}-(3p) = −6.5 eV, ζ(3s) = ζ(3p) = 1.167.

Results and Discussion

In the following discussion, we summarize the experimental and theoretical results relevant to an understanding of how Mg, Zn, and Al distribute themselves in the cubic R-phase structure. Although there are other examples adopting this structure type in the literature,^{26,54–58} these results comprise the first thorough investigation of a ternary system that shows a phase width for this structure. Furthermore, to elucidate the distribution of elements in this structure, not only were detailed structural assessments necessary, but thorough elemental analyses of single-crystal and bulk samples were crucial to reach the conclusions. The final model, which we present in the next section, relies on using a combination of diffraction methods, density measurements, and elemental analyses.

Structure Determination. (i) Structure. The body-centered-cubic, R-phase structure adopted by several examples in the Mg–Zn–Al system involves seven crystallographic sites (A1–A3 and M1–M4; these labels are selected to reflect the results of evaluating the atomic site distributions) that form three shells of polyhedra containing 12, 32, and 60 vertices surrounding the center and corners of the cubic unit cell with additional A atoms filling voids as the 60-vertex polyhedra condense to form the three-dimensional structure. A perspective view of this structure along the [100] direction is shown in Figure 2. This structure is one of three types adopted by group 13 intermetallic compounds with large polyhedra as building units: (1) the cubic (R-phase) structure, e.g. Mg_{2–3}(Zn,Al)_{3+y},²⁶ Li₃CuAl₅,⁵⁴ Li₁₃-Cu₆Ga₂₁,⁵⁵ Na₁₃Cd₂₀E₇ (E = Pb, Sn),⁵⁶ K₄₉Tl₁₀₈,⁵⁷ (2) the hexagonal (stuffed boron) structure, e.g., K₃₄Zn₂₀In₈₅,⁵⁸ Na₁₇-Zn₁₂Ga_{40.5},⁵⁹ and (3) condensed fullerene-like cage structures, e.g., LiMgAl₂,^{3,60} Na₉₆In₉₇Z₂ (Z = Ni, Pd, Pt),⁶¹ and Na_{~172}-

(46) Mulay, L. N.; Boudreaux, E. A. *Theory and Applications of Molecular Diamagnetism*; Wiley: New York, 1976.

(47) Hoffmann, R.; Lipscomb, W. N. *J. Chem. Phys.* **1962**, *36*, 2179; 3489.

(48) Hoffmann, R. *J. Chem. Phys.* **1963**, *39*, 1397.

(49) Ammeter, J. H.; Buerger, H. B.; Thibeault, J. C.; Hoffmann, R. *J. Am. Chem. Soc.* **1978**, *100*, 3686–3692.

(50) Whangbo, M.-H.; Hoffmann, R.; Woodward, R. B. *Proc. R. Soc. London, Ser. A* **1979**, *366*, 23–46.

(51) Hughbanks, T.; Hoffmann, R. *J. Am. Chem. Soc.* **1983**, *105*, 3528–3537.

(52) Wijeyesekera, S. D.; Hoffmann, R. *Organometallics* **1984**, *3*, 949–961.

(53) Chadi, D. J.; Cohen, M. L. *Phys. Rev. B* **1973**, *8*, 5474.

(54) Audier, M.; Pannetier, J.; Leblanc, M.; Janot, C.; Lang, J.-M.; Dubost, B. *Physica B* **1988**, *153*, 136.

(55) Tillard-Charbonnel, M.; Belin, C. *J. Solid State Chem.* **1991**, *90*, 270–278.

(56) Todorov, E.; Sevov, S. C. *Inorg. Chem.* **1997**, *36*, 4298.

(57) Cordier, G.; Mueller, V. Z. *Naturforsch., B* **1993**, *48*, 1035–1040.

(58) Cordier, G.; Mueller, V. Z. *Naturforsch., B* **1995**, *50*, 23–30.

(59) Tillard-Charbonnel, M.; Chouaibi, N. E.; Belin, C. *C. R. Acad. Sci., Ser. II* **1992**, *315*, 661–5.

(60) Nesper, R. *Angew. Chem., Int. Ed. Engl.* **1994**, *33*, 843.

(61) Sevov, S. C.; Corbett, J. D. *Science (Washington, D.C.)* **1993**, *262*, 880–388.

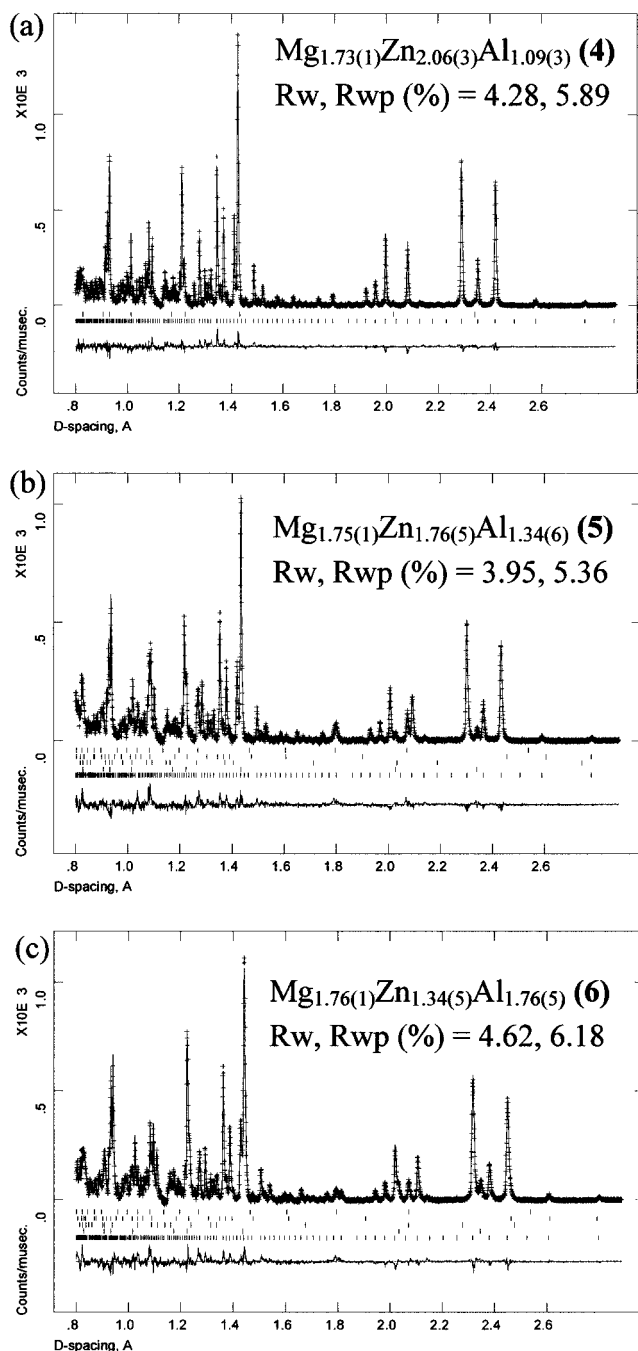


Figure 1. Observed (+) and refined powder neutron diffraction profiles (solid line) of samples (a) **4**, (b) **5**, and (c) **6** from Rietveld refinements. The refined compositions for each sample are labeled on each plot, and the Bragg peaks (R-phase and impurities) are noted by tic marks below each profile. A difference curve (raw data minus calculated data) is shown at the bottom, and a background correction has been applied to each curve.

$\text{In}_{\sim 197}\text{Z}_2$ ($Z = \text{Ni, Pd}$).⁶² Derivative structures of these three types also exist but may be considered superstructures, such as $\text{Z-Al}_{59}\text{Cu}_5\text{Li}_{26}\text{Mg}_{10}$, which is related to the R-phase.⁶³ Although each structure type is different, the atomic networks contain common polyhedral building blocks such as icosahedra and truncated tetrahedra (Friauf polyhedra).⁶⁴ In the following

(62) Sevov, S. C.; Corbett, J. D. *J. Solid State Chem.* **1996**, *123*, 344–370.

(63) Le Bail, A.; Leblanc, M.; Audier, M. *Acta Crystallogr., Sect. B: Struct. Sci.* **1991**, *B47*, 451–457.

(64) Friauf, J. B. *J. Am. Chem. Soc.* **1927**, *49*, 3107–3114.

discussion, the distances reported are for Mg–Zn–Al systems in our study.

The first shell of atoms is an icosahedron of 12 M2 atoms with a radius of 2.53(1) Å and M2–M2 distances between 2.63 and 2.68 Å. No atomic density is detected at the center of the cluster (Wyckoff site 2a) according to both X-ray and neutron diffraction experiments, which disagrees with the original report for $\text{Mg}_{32}(\text{Zn,Al})_{49}$ by Pauling and Bergman,^{26,27} who assigned this site to be 80% Al. (Note: while we were finishing this manuscript, an abstract of a report of an X-ray diffraction study of crystalline $\text{Mg}_{32}(\text{Zn,Al})_{49}$ indicated the same result as ours,⁶⁵ and a similar conclusion was also achieved for a Na–Mg–Zn–Al R-phase.⁶⁶)

The second shell of atoms contains a large icosahedron of 12 M1 sites and a pentagonal dodecahedron of 8 A2 sites and 12 A3 atoms, which together form a 32-vertex triacontahedron. Each M1 atom is connected to a vertex of the inner M2 icosahedron at distances between 2.53 and 2.56 Å (the radius of the M1 icosahedron is 5.06(2) Å). Each of the 20 A2 and A3 atoms caps a triangular face of the inner M2 icosahedron (the radius of the pentagonal dodecahedron is 5.61(3) Å). The average A–M1 and A–M2 distances are, respectively, 3.20(2) and 3.02(1) Å.

The third shell of atoms contains 48 M3 sites and 12 M4 sites to form a buckminsterfullerene-type polyhedron (truncated icosahedron) with an average radius of 6.88(5) Å. Every atom on the third shell is shared with the third shell of an adjacent unit: M3 atoms are shared along the {111} directions, and M4 sites are shared along the {100} directions.

The M1–M4 sites form a large M_{84} cluster called a Samson polyhedron.⁶⁷ The A1 sites occupy all “tetrahedral holes” created by the body-centered condensed packing of these Samson polyhedra, shown in Figure 3. The local environment is a 13-vertex Friauf-type polyhedron around each A1 atom. Finally, with respect to the seven crystallographic sites in the R-phase structure, the general formula can be written as

$$\begin{aligned} & \{[(\text{M}2)_{12}(\text{M}1)_{12}(\text{A}2)_8(\text{A}3)_{12}][(\text{M}3)_{48/2}(\text{M}4)_{12/2}]\}(\text{A}1)_{2/4} \\ & \equiv \text{A}_{26}\text{M}_{54} = \text{A}_{1.625}\text{M}_{3.375} \end{aligned}$$

(ii) Site Occupancies. In the Mg–Zn–Al system, it is difficult to distinguish Mg and Al unequivocally using the results of electron density distributions from X-ray diffraction data. On the other hand, the coherent scattering lengths⁶⁸ for Mg (5.375 fm), Al (3.449 fm), and Zn (5.680 fm) allow excellent differentiation of Mg and Al, but now a problem in resolving Mg from Zn emerges. Nevertheless, the metallic radii of Mg, Al, and Zn for coordination number 12 are, respectively, 1.60, 1.43, and 1.37 Å, which are sufficiently different to allow atomic assignments on the basis of (1) interatomic distances and (2) coordination environments of each site. The final structural model from both single-crystal X-ray and powder neutron diffraction, which takes these distance criteria into account, divides the seven atomic sites into three distinct sets: (1) three sites occupied solely by Mg atoms (A1, A2, and A3), (2) three mixed-occupied sites involving Zn and Al (M1, M2, and M3), and (3) one site (labeled M4) that could involve any assortment

(65) Sun, W.; J., L. F.; Sugiyama, K.; Hiraga, K. *Structure of Al, Zn*₄₉*Mg*₃₂-type phase by single-crystal X-ray diffraction: Abstract PB23 from 7th International Conference on Quasicrystals, Stuttgart, Germany, 1999; p 37.

(66) Elding-Ponten, M.; Lidin, S. *J. Solid State Chem.* **1995**, *115*, 270–273.

(67) Samson, S. In *Structure Chemistry and Molecular Biology*; Rich, A., Davidson, N., Eds.; Freeman: San Francisco, 1968; pp 687–717.

(68) Sears, V. F. *Neutron News* **1992**, *3*, 26.

Table 6. Crystallographic Data for “Mg_{1.63}Zn_xAl_{1-x}” from Neutron Powder Diffraction

reactions refined composition	Mg _{1.63} Zn _{2.16} Al _{1.21} Mg _{1.73(1)} Zn _{2.06(3)} Al _{1.09(3)} (4)	Mg _{1.63} Zn _{1.72} Al _{1.65} Mg _{1.75(1)} Zn _{1.76(5)} Al _{1.34(6)} (5)	Mg _{1.63} Zn _{1.21} Al _{2.16} Mg _{1.76(1)} Zn _{1.34(5)} Al _{1.76(5)} (6)
space group, <i>Z</i>	<i>Im</i> $\bar{3}$, 32	<i>Im</i> $\bar{3}$, 32	<i>Im</i> $\bar{3}$, 32
color	gray powder	gray powder	gray powder
temperature, K	10(2)	10(2)	10(2)
formula wt (g/mol)	6.6(1) × 10 ³	6.2(2) × 10 ³	5.7(1) × 10 ³
<i>a</i> (Å)	14.11247(6)	14.1804(1)	14.2697(1)
<i>V</i> (Å ³)	2810.66(2)	2851.48(5)	2905.66(4)
<i>d</i> _{calc} (g/cm ³)	3.90(6)	3.62(9)	3.25(6)
<i>d</i> _{exp} (g/cm ³)	4.10(3)	3.75(4)	3.4(1)
scattering angle (deg)	145.88	145.88	145.88
<i>d</i> -spacing range, Å	0.8–2.8	0.8–2.8	0.8–2.8
no. of data points	4335	4335	4335
no. of Bragg reflections	610	687	689
no. of parameters	53	56	56
<i>R</i> _p , <i>R</i> _{wp} (%)	4.28, 5.89	3.95, 5.36	4.62, 6.18
goodness-of-fit (χ) ^b	1.43	1.53	1.71

^a $R_p = \sum |Y_o| - |Y_c| / \sum |Y_o|$; $R_{wp} = [\sum [w(Y_o^2 - Y_c^2)^2] / \sum [w(Y_o^2)^2]]^{1/2}$; Y_o and Y_c are observed and calculated counts. ^b $\chi = [\sum [w(Y_o^2 - Y_c^2)^2] / (N_{obs} - N_{var})]^{1/2}$; N_{obs} is the number of observations and N_{var} is the number of parameters.

Table 7. Atomic Positions, U_{eq} (×100 Å²)^a and Site Occupancies for Refined Structures of Mg_{1.73(1)}Zn_{2.06(3)}Al_{1.09(3)} (4), Mg_{1.75(1)}Zn_{1.76(5)}Al_{1.34(6)} (5), and Mg_{1.76(1)}Zn_{1.34(5)}Al_{1.76(5)} (6) from Neutron Powder Diffraction

atom	site	<i>x</i>	<i>y</i>	<i>z</i>	<i>U</i> _{eq}	site occ.
Mg _{1.73(1)} Zn _{2.06(3)} Al _{1.09(3)} (4)						
A1	12e	0.2022(3)	1/2	0	0.94(8)	Mg 1.00(1)
A2	16f	0.1861(2)	0.1861(2)	0.1861(2)	0.93(8)	Mg 1.00(1)
A3	24g	0.1190(2)	0.3011(2)	0	0.75(5)	Mg 1.00(1)
M1	24g	0.3100(2)	0.1772(2)	0	0.76(5)	Al 0.48(1) Zn 0.52(1)
M2	24g	0.1527(2)	0.0941(3)	0	0.77(5)	Al 0.25(1) Zn 0.75(1)
M3	48h	0.3137(2)	0.3411(2)	0.0962(2)	0.79(4)	Al 0.36(1) Zn 0.64(1)
M4	12e	0.4075(4)	1/2	0	0.7(1)	Mg 0.27(2) Zn 0.40(1)
Mg _{1.75(1)} Zn _{1.76(5)} Al _{1.34(6)} (5)						
A1	12e	0.1970(5)	1/2	0	1.0(1)	Mg 1.00(2)
A2	16f	0.1866(2)	0.1866(2)	0.1866(2)	1.0(1)	Mg 1.00(2)
A3	24g	0.1191(3)	0.2999(3)	0	1.08(8)	Mg 1.00(1)
M1	24g	0.3090(4)	0.1769(3)	0	0.62(9)	Al 0.53(2) Zn 0.47(2)
M2	24g	0.1516(3)	0.0933(4)	0	0.69(9)	Al 0.14(2) Zn 0.86(2)
M3	48h	0.3132(3)	0.3396(3)	0.0971(3)	0.73(7)	Al 0.56(2) Zn 0.44(2)
M4	12e	0.4076(7)	1/2	0	0.7(2)	Mg 0.34(2) Zn 0.28(1)
Mg _{1.76(1)} Zn _{1.34(5)} Al _{1.76(5)} (6)						
A1	12e	0.1944(7)	1/2	0	1.0(1)	Mg 1.00(1)
A2	16f	0.1852(2)	0.1852(2)	0.1852(2)	1.0(1)	Mg 1.00(1)
A3	24g	0.1177(4)	0.2994(4)	0	1.14(7)	Mg 1.00(1)
M1	24g	0.3084(4)	0.1805(4)	0	0.82(8)	Al 0.70(2) Zn 0.30(2)
M2	24g	0.1515(3)	0.0924(4)	0	0.74(8)	Al 0.27(2) Zn 0.73(2)
M3	48h	0.3103(3)	0.3415(4)	0.0972(4)	0.82(6)	Al 0.69(1) Zn 0.31(1)
M4	12e	0.4045(8)	1/2	0	0.8(2)	Mg 0.35(2) Zn 0.27(1)

$$^a U_{eq} = (1/3) \sum_i \sum_j U_{ij} a^i a^j a_k$$

of Zn, Al, Mg, and vacancies. In the Bergman and Pauling model, the M4 site is exclusively assigned to Mg atoms.

Atomic site occupancies were first refined on each independent crystallographic site. The Mg sites (A1, A2, and A3) remained essentially unchanged (variations were less than 2%) and were fixed at 100% Mg for all subsequent single-crystal and powder refinements. The compositions of the other metal sites (M1–M4) were then refined using constrained fractional

Table 8. Bond Lengths (Å) for Mg_{1.73(1)}Zn_{2.06(3)}Al_{1.09(3)} (4), Mg_{1.75(1)}Zn_{1.76(5)}Al_{1.34(6)} (5), and Mg_{1.76(1)}Zn_{1.34(5)}Al_{1.76(5)} (6) with Estimated Standard Deviations in Parentheses

		4	5	6
A1	A3 (2×)	3.039(3)	3.046(4)	3.073(4)
	M1 (4×)	3.179(4)	3.245(6)	3.259(6)
	M3 (4×)	3.060(4)	3.128(6)	3.124(6)
	M3 (4×)	3.021(3)	3.031(4)	3.084(4)
A2	M4	2.898(7)	2.99(1)	3.00(1)
	M4 (2×)	3.136(5)	3.086(8)	3.103(7)
	A2	3.114(7)	3.12(1)	3.198(9)
	A3 (3×)	3.232(2)	3.240(3)	3.254(3)
A3	M1 (3×)	3.158(2)	3.168(3)	3.179(3)
	M2 (3×)	2.972(3)	2.999(5)	2.999(4)
	M3 (3×)	3.102(3)	3.089(5)	3.116(5)
	M3 (3×)	3.092(3)	3.089(5)	3.123(5)
M1	A3	3.361(6)	3.38(1)	3.350(9)
	M1	3.212(4)	3.209(7)	3.228(7)
	M1 (2×)	3.016(3)	3.027(5)	3.058(4)
	M2	2.964(4)	2.965(6)	2.995(6)
M2	M2 (2×)	2.994(4)	3.003(5)	3.006(4)
	M3 (2×)	3.117(4)	3.129(6)	3.145(6)
	M3 (2×)	3.052(2)	3.082(4)	3.133(4)
	M4 (2×)	3.522(3)	3.552(5)	3.577(5)
M3	M2	2.508(5)	2.527(8)	2.571(7)
	M3 (2×)	2.684(4)	2.687(6)	2.697(5)
	M3 (2×)	2.606(3)	2.639(5)	2.638(5)
	M4	2.935(4)	2.962(6)	2.985(5)
M4	M2	2.665(3)	2.657(5)	2.660(4)
	M2 (4×)	2.652(7)	2.65(1)	2.634(9)
	M3	2.718(5)	2.755(9)	2.781(8)
	M3 (2×)	2.678(2)	2.668(4)	2.679(4)
M4	M4	2.934(4)	2.977(6)	2.988(6)
	M4	2.62(1)	2.62(2)	2.69(2)

occupancies of Zn and Al. To determine the final “composition” (i.e., average electron density or elastic scattering length) on each M1–M4 site, three different initial Zn:Al ratios (0:100, 50:50, and 100:0) were assigned on each individual site to be refined. For each sample, these refinements for each Zn/Al site gave the same final composition, and the thermal displacement parameters for all atomic sites could be refined anisotropically.

Figure 4 illustrates the results of refinements of the M1–M4 sites in two plots: (1) from single-crystal X-ray diffraction, the average electron density for each site vs lattice constant and (2) from powder neutron diffraction, the average elastic scattering factor for each site vs lattice constant. The occupation of the M2 site remains essentially constant and Zn rich for all examples. Since the interatomic M2–M2 and M2–M1 distances are appropriate just for Zn or Al, we assign M2 as a mixture of Al and Zn, which refines to 83(3)% Zn for all compositions.

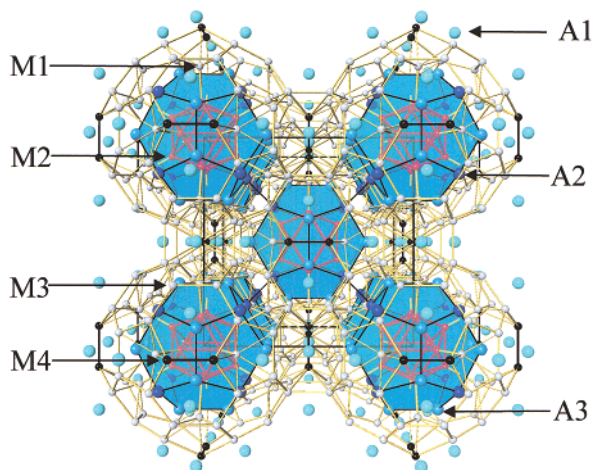


Figure 2. Crystal structure (ATOMS 5.0) of the R-phase structure for $\text{Mg}_{2-y}(\text{Zn}_x\text{Al}_{1-x})_{3+y}$ projected in perspective along [100]. The Mg atoms (A1, A2, A3) are drawn as blue circles; the M1, M3, and M4 atoms are drawn as small circles with different gray scales; the M2 atoms are drawn as red circles. Yellow, red, and black lines indicate M–M contacts with distances less than 3.10 Å. A_{20} pentagonal dodecahedra are represented in blue.

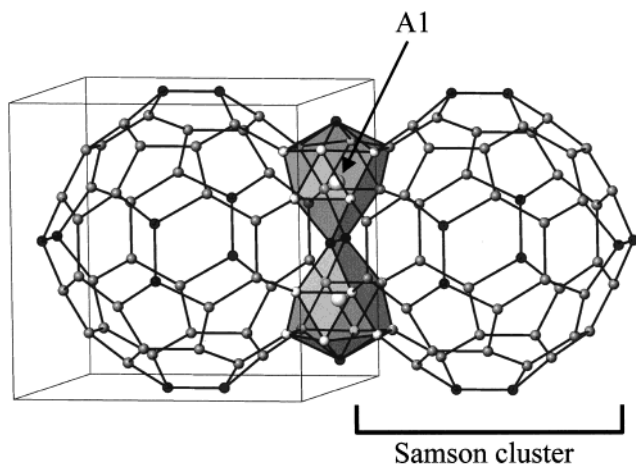


Figure 3. A1 crystallographic site in the R-phase structure. The outer shell of the Samson polyhedron and the 13-vertex coordination environment for the A1 site are emphasized.

The average formula of the M2 icosahedron, therefore, is close to $[\text{Zn}_{10}\text{Al}_2]$ (83.3% Zn), which is similar to a NaZn_{13} -type compound, $\text{BaZn}_{10}\text{Al}_2$.⁶⁹ These two independent results suggest that the $[\text{Zn}_{10}\text{Al}_2]$ icosahedron is a stable building unit in these intermetallic phases. The M1 and M3 sites increase in Zn content as the lattice constant decreases. According to the distance criteria, therefore, these two sites are also assigned as mixtures of Zn and Al, which change composition by identical relations with total composition of the sample (M1 varies from 19.5–(4)% to 72.0(6)% Zn; M3 varies from 19.7(4)% and 73.2(5)% Zn). The composition of the M4 site is nearly insensitive for all samples except at low lattice constants, but neither X-ray nor neutron diffraction results lead to a single conclusion. Nevertheless, the combination of these experimental results strongly suggests that Mg and Zn atoms occupy this site. Other than the M4–M4 distances (2.6–2.7 Å), all other contacts to the M4 site exceed 2.90 Å. Therefore, if a Mg atom occupies one M4 site, we hypothesize that the adjacent M4 site must be vacant. To reach a definite conclusion, we need to incorporate results from additional elemental analyses.

(69) Lee, C.-S.; Miller, G. J. Manuscript in preparation.

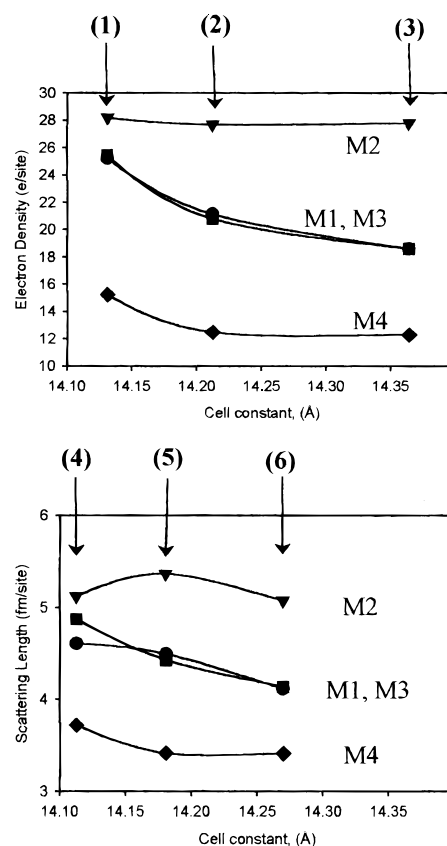


Figure 4. (Top) Refined electron densities vs lattice constants for the M1–M4 sites from single-crystal X-ray diffraction experiments for three samples, 1, 2, and 3. (Bottom) Refined elastic scattering lengths vs lattice constants for the M1–M4 sites from powder neutron diffraction experiments for three samples, 4, 5, and 6.

Table 9. Models of $\text{Mg}_{52}(\text{Al}_w\text{□}_{1-w})_{12}\text{Al}_{96}$ ($w = 0-1$)^a

model	formula	M4–M4 contact		
		Al–Al	Al–□	□–□
I	$\text{Mg}_{52}(\text{□}_{12}\text{Al}_0)\text{Al}_{96}$	0	0	6
II	$\text{Mg}_{52}(\text{□}_8\text{Al}_4)\text{Al}_{96}$	2	0	4
III	$\text{Mg}_{52}(\text{□}_8\text{Al}_4)\text{Al}_{96}$	0	4	2
IV	$\text{Mg}_{52}(\text{□}_6\text{Al}_6)\text{Al}_{96}$	0	6	0
V	$\text{Mg}_{52}(\text{□}_4\text{Al}_8)\text{Al}_{96}$	4	0	2
VI	$\text{Mg}_{52}(\text{□}_4\text{Al}_8)\text{Al}_{96}$	2	4	0
VII	$\text{Mg}_{52}(\text{□}_0\text{Al}_{12})\text{Al}_{96}$	6	0	0

^a □ denotes a vacancy on the M4 site.

Elemental Analysis. The results of EDS analyses performed on three different single-crystal samples (used for single-crystal X-ray diffraction) and three bulk samples (used for powder neutron diffraction) are summarized in Table 5. In every case except one bulk sample, the Mg content exceeds 32.5 at. % (52 Mg atoms on the A1–A3 sites out of 160 total sites in the unit cell). Furthermore, the Mg content never reaches 40.0 at. % (64 Mg atoms on the A1–A3 and M4 sites) but monotonically increases as the Al content increases. In addition to the analytical results, the experimental densities for the three bulk samples are also listed in Table 5 and are consistent with the analytical results.

To reach conclusions for the final compositions at the M4 sites in these R-phase structures, we carried out seven different refinement strategies of the X-ray and neutron diffraction data to achieve the best overall agreement with the elemental analysis and density. These models involved refining the M4 site for occupation by (1) Mg only, (2) Zn only, (3) Al only, (4) a mixture of Mg and Zn, (5) a mixture of Mg and Al, (6) a mixture

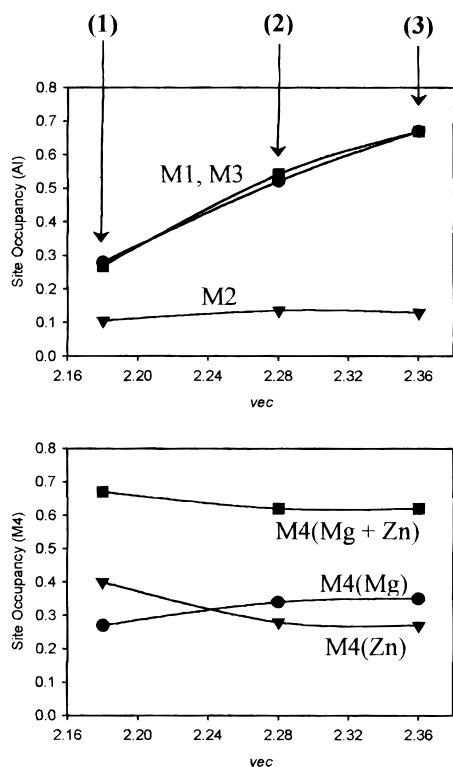


Figure 5. Variations in site occupancies by Zn vs valence electron concentration (VEC).

of Zn and Al, and (7) a mixture of Mg, Al, and Zn. The model that provided the best overall agreement with all data for all samples was (4), refining a mixture of Mg and Zn at the M4 site. The total occupancies for each sample refine to ca. 67%, so that 33% of the M4 sites remain vacant. These results of the “analysis” from refinements of single-crystal X-ray diffraction and powder neutron diffraction experiments are also listed in Table 5 for comparison with EDS measurements. Furthermore, the various site occupancies from this model are included in Tables 3 (X-ray diffraction) and 7 (neutron diffraction) and plotted with respect to VEC in Figure 5. These refinements show that the M4 site is approximately 33% Zn, 33% Mg, and 33% vacancies. Since the M4 site has 12 positions in the unit cell, there are four vacancies (on average) per unit cell. Among the eight remaining sites, we hypothesize four Mg adjacent to vacancies and four Zn atoms forming two Zn–Zn pairs. In the section on theoretical calculations, we describe a model to account for this pattern of site occupancies and the presence of vacancies.

Phase Width Investigations. Table 1 summarizes the results of powder and single-crystal studies as well as DTA measurement on $\text{Mg}_{2-y}(\text{Zn}_x\text{Al}_{1-x})_{3+y}$ samples for $y = 0.33$ and 0.40 , $0 \leq x \leq 1$. According to X-ray powder diffraction patterns, the R-phase was observed for x between 0.19 (VEC = 2.55) and 0.74 (VEC = 2.18). Mixtures of an R-phase and other binary or elemental phases were observed for $x < 0.41$ (VEC > 2.40) and $x > 0.63$ (VEC < 2.25) reactions. Also, no binary phase adopting the R-phase structure was found. For $0.41 < x < 0.63$ ($2.25 < \text{VEC} < 2.40$), nearly single-phase products were identified. DTA experiments on “ $\text{Mg}_{1.625}\text{Zn}_{1.375}\text{Al}_{2.0}$ ”, which is the single-phase sample with the highest Al content, revealed a congruently melting sample, with endothermic and exothermic events observed, respectively, at 780.1 (heating) and 768.7 K (cooling). X-ray powder diffraction patterns from this sample, taken before and after the DTA measurements, showed no decomposition of the sample.

Physical Properties. The “ $\text{Mg}_{1.625}\text{Zn}_{1.688}\text{Al}_{1.688}$ ” polycrystalline sample shows metallic behavior ($d\rho/dT > 0$) throughout the temperature range 1.8–300 K, and its room-temperature resistivity of $62.5 \mu\Omega\cdot\text{cm}$ is higher than resistivities reported for each of the component elements, Mg ($4.45 \mu\Omega\cdot\text{cm}$), Zn ($5.9 \mu\Omega\cdot\text{cm}$), and Al ($2.65 \mu\Omega\cdot\text{cm}$).⁷⁰ Furthermore, this resistivity value is close to reports of room-temperature resistivities of the quasicrystalline phases, $i\text{-Mg}_{32}(\text{Zn}_x\text{Al}_{1-x})_{49}$ ($x = 0.50$ and 0.69), which are, respectively, 59(5) and 90(10) $\mu\Omega\cdot\text{cm}$.³¹ In addition, magnetic susceptibility measurements at 3 T for “ $\text{Mg}_{1.625}\text{Zn}_{1.375}\text{Al}_{2.00}$ ”, “ $\text{Mg}_{1.625}\text{Zn}_{1.688}\text{Al}_{1.688}$ ”, and “ $\text{Mg}_{1.625}\text{Zn}_{2.125}\text{Al}_{1.25}$ ” demonstrate Pauli paramagnetic behavior, which is also consistent with metallic character.

Theoretical Calculations. Figure 6 illustrates the DOS and COOP curves for the R-phase structure using the atomic orbital parameters associated with the model $\text{Mg}_{52}\text{Al}_{108}$ ($A_{52}M_{108}$). The Fermi energy (E_F) calculated to give the optimized total bonding within the M1–M4 network (as given by the total overlap population for all M–M interactions) is indicated by the dashed line.

The DOS curve shows no band gap within the VEC range between 2.07 and 2.25 e^-/atom ($-7.8 \text{ eV} \leq E_F \leq -6.1 \text{ eV}$), although this region has significantly lower DOS values than the surrounding energy regions, which is consistent with the resistivity measurements on the Mg–Zn–Al phases. According to the COOP curve, this part of the DOS is nearly nonbonding for the total M–M interaction (the total overlap population varies by less than 0.6% throughout the range). The peak between -8 and -10 eV comes mostly from Al 3p orbitals, while below this peak, the DOS curve is featureless and approximates a nearly free electron distribution of electronic states.

The total overlap population of the $^3[M_{108}]$ network is maximized at VEC = 2.18 e^-/atom . The overlap populations of individual M–M contacts, however, indicate optimal bonding interactions at different VEC values for each contact, which agrees with the computational results on $\text{Na}_{13}\text{Cd}_{20}\text{Pb}_7$ (these calculations were performed without atomic orbitals at the Na (A) positions).⁵⁶ The M2–M2 contacts in the first shell and the M1–M4 contacts between the second and third shells are optimized at VEC = 2.14 e^-/atom . Other inter-shell contacts, viz., M1–M2 and M1–M3, are optimized, respectively, at VEC = 2.36 and 2.20 e^-/atom . Within the third shell, the largest overlap populations for M3–M3, M3–M4, and M4–M4 interactions are observed at VEC = 2.29, 2.25, and 2.50 e^-/atom , respectively. Therefore, to optimize various M–M interactions in the R-phases, values of the VEC should range between 2.14 and 2.50 e^-/atom . These results are in good agreement with the observed range of VEC values in the single-crystal study (VEC = 2.17–2.41 e^-/atom). Like the total overlap population for all M–M interactions in this structure, each M–M contact shows essentially nonbonding character between -6.1 and -7.8 eV . These results suggest that the VEC can be varied without significantly changing the bond strength of the M–M contacts by adjusting the molar ratio of Zn to Al and, therefore, producing an observable phase width (i.e., variable x) in $\text{Mg}_{2-y}(\text{Zn}_x\text{Al}_{1-x})_{3+y}$.

This distinctive, nonbonding region ($2.07 < \text{VEC} < 2.25$) in the DOS, however, is nonzero. Decompositions of the total DOS into contributions from each of the M1–M4 sites are illustrated in Figure 7. From these results, we can now understand the trends between site preference and x in

(70) Ashcroft, N. W.; Mermin, N. D. *Solid State Physics*; Saunders College Publishing: Orlando, 1976.

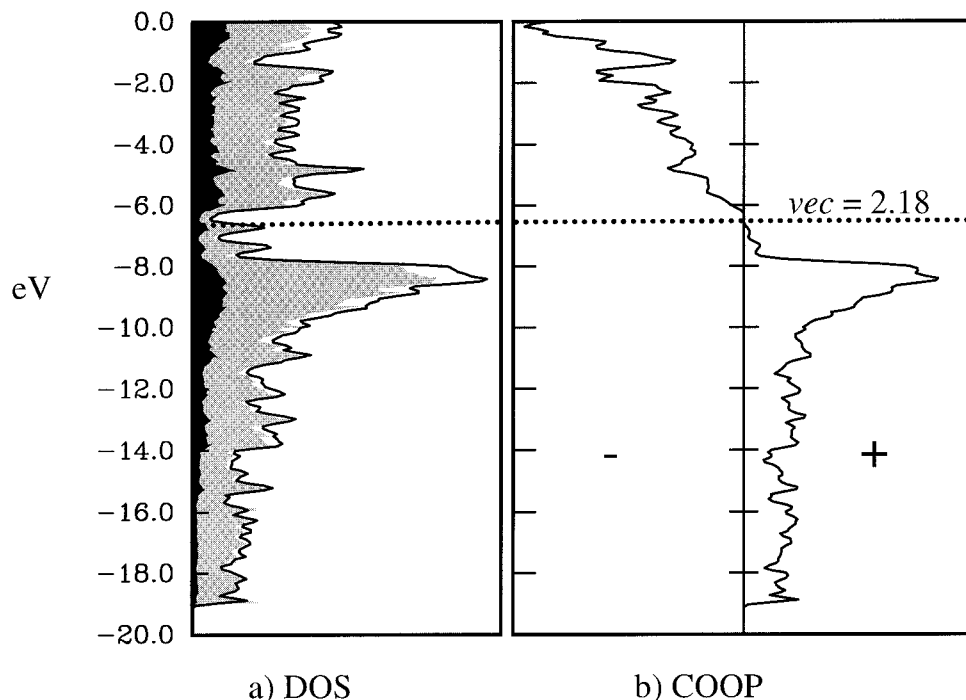


Figure 6. (a) Total density of states (solid line) and partial DOS curves (PDOS) of Mg (black) and Al (gray) for the R-phase model “Mg₅₂Al₁₀₈”. (b) COOP curve for all Al–Al contacts less than 3.10 Å. The dashed line indicates the Fermi level for VEC = 2.18, the value at which the total Al–Al overlap population is optimized.

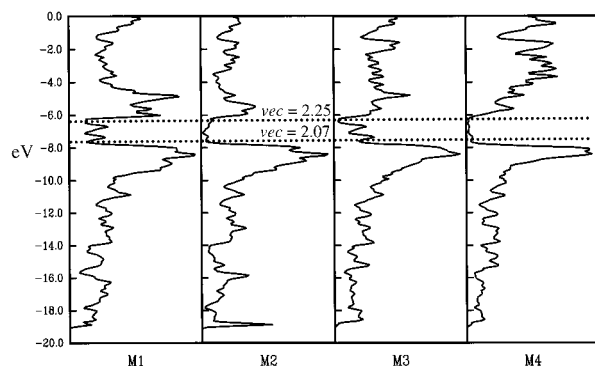


Figure 7. PDOS curves for the M1, M2, M3, and M4 sites from the results of EHT calculations. The dashed lines indicate the minimum and maximum Fermi energies ($2.07 \leq \text{VEC} \leq 2.25$) for which the M–M contacts show essentially nonbonding interactions.

Mg_{2-y}(Zn_xAl_{1-x})_{3+y} that are shown in Figure 5. These DOS curves indicate the following:

(1) The Mulliken populations (MPs) of the M1 and M3 sites are sensitive to VEC across this nonbonding range (the variations of MPs are 10% for M1 and 11% for M4). Therefore, the chemical compositions of these two sites will change when the VEC is altered.

(2) The M2 and M4 sites essentially do not contribute to the electronic states in this nonbonding region of the DOS. The MPs at these two sites, therefore, remain constant for changes in VEC (the MPs for M2 and M4 increase by 4% and 2%, respectively, across the range). Therefore, as the VEC of the Mg–Zn–Al R-phase is varied by changing the Zn:Al molar ratio, the chemical composition of the M2 and M4 sites should remain nearly fixed in this VEC region. When VEC exceeds 2.25 e⁻/atom, the M2 and M4 sites contribute orbitals to the total DOS, and the chemical compositions at these sites will begin to change. The values of the MPs for the M2 (2.4–2.5) and M4 (2.3–2.4) sites also agree with the diffraction results:

the M2 site attracts more Zn (the most electronegative element) than the M4 site.

The best model that accounts for our diffraction and analytical data places four vacancies per unit cell at the M4 site. Our theoretical calculations have shown that M–M bonding in the A₅₂M₁₀₈ model is optimized at VEC = 2.18 e⁻/atom, which is close to the “magic number” of electrons for this structure predicted by King (340 e⁻/unit cell or VEC = 2.125 e⁻/atom).⁷¹ Increasing the VEC by increasing the Al content will push the Fermi level up to some M–M antibonding orbitals once the VEC exceeds ca. 2.25 e⁻/atom, according to a rigid band model applied to the DOS and COOP curves in Figure 6. To alleviate such antibonding interactions, extended solids can either undergo a structural distortion (e.g., the puckering of the honeycomb network in α-As⁷²) or create vacancies in the network. In the R-phase structure, therefore, a model with vacancies incorporated into the network becomes favored. Figure 8 illustrates the trend in total valence electron energy per atom with changes in the average number of valence electrons per atom for various vacancy models at the M4 site in the R-phase structure, i.e., Mg₅₂(Al_w□_{1-w})₁₂Al₉₆. When VEC exceeds ca. 2.28 e⁻/atom, structural models with vacancies in the M4 position become preferred. According to our simple model, there is a narrow range of stability ($2.28 < \text{VEC} < 2.33$) for four vacancies per unit cell. For larger VEC values, six vacancies per unit cell are favored. The seven structural models we examined are summarized in Table 9, which also describes how the vacancies are distributed in each model: since the M4 position involves six M4–M4 pairs, vacancies can occur either together (□–□) or isolated (M–□).

This argument is similar to accounting for vacancies in the network of tetrahedral semiconductors using the Grimm–Sommerfeld valence rule or for “missing” cluster atoms in carborane deltahedra using Wade’s rules.⁷² For tetrahedral

(71) King, R. B. *Inorg. Chim. Acta* **1991**, *181*, 217–225.

(72) Burdett, J. K. *Molecular Shapes: Theoretical Models of Inorganic Stereochemistry*; Wiley: New York, 1980.

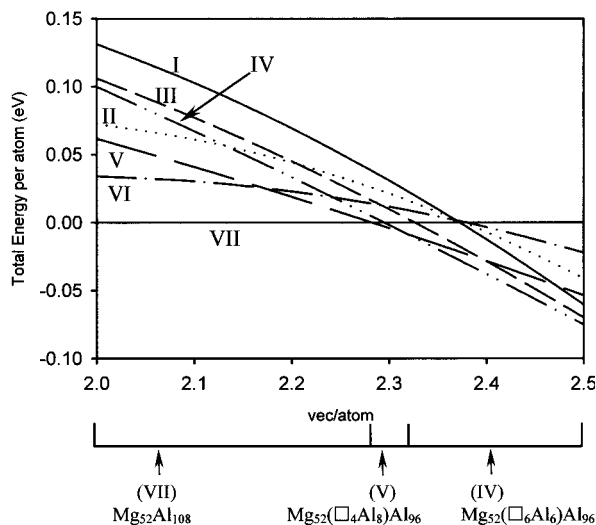


Figure 8. Variations in total energy per atom with VEC for various R-phase models including vacancies at the M4 sites. The seven models are summarized in Table 9. Below the graph, the lowest energy vacancy model is labeled over the range of VEC plotted.

frameworks, the average valence electron count *per site* is four; if there are vacancies in the structure, the valence electron count *per atom* (i.e., VEC) is greater than four. In carborane chemistry, a *closo*-deltahedron with n cluster atoms needs $n + 1$ pairs of skeletal electrons. The *nido*-cluster based upon the same deltahedron needs the same number of skeletal electron pairs but has *one less atom*. Therefore, VEC increases from *closo*- to *nido*- (and to *arachno*-) deltahedra.

R-Phase Mg–Zn–Al: Where Are the Atoms? All data from X-ray and neutron diffraction as well as EDS and density measurements lead to the general formulation for the Mg–Zn–Al R-phases as $\text{Mg}_{52}[(\text{Mg}_v\text{Zn}_u\text{Al}_w\text{Al}_2)_{12}(\text{Zn}_w\text{Al}_{1-w})_{96}]$, in which the occupancy of the 12-fold M4 site is emphasized. According to this formulation, the valence electron count per site is $2.45 + 0.15(u + v) - 0.6w$; $u + v$ represents the total fraction of M4 sites occupied and w is the fraction of Zn on the remaining 96 M1–M3 sites. The range in VEC observed for Mg–Zn–Al phases exceeds the values appropriate for complete occupation of all crystallographic sites and thus leads to the creation of vacancies. In this ternary system, the Al content must be less than ca. 20 at. % to eliminate vacancies ($w > 0.67$ with $u + v = 1$), but these synthetic targets, e.g., “ $\text{Mg}_{52}(\text{Mg}_u\text{Zn}_v)_{12}(\text{Zn}_{0.90}\text{Al}_{0.10})_{96} = \text{Mg}_{1.625+0.375u}\text{Zn}_{2.70+0.375v}\text{Al}_{0.30}$ ”, will compete against the formation of MgZn_2 . Nevertheless, the report of quasicrystalline phases in the Mg–Zn–Al systems obtained by splat-quenching melted mixtures of these elements suggests that quasicrystalline structures may arise when such vacancies are eliminated.

Figure 9a shows a fragment of the crystalline R-phase containing three shells of M1–M4 sites and two shells of the A sites (A1–A3 sites) projected along a pseudo-5-fold axis, $[3^{1/2}, 1, 0]$, of the cluster. The point group of this fragment is T_h based on the space group of $Im\bar{3}$, which is the highest point symmetry allowed for an icosahedron in a crystalline structure. Figure 9b illustrates the same type of fragment, but with I_h point symmetry. In this model, each shell of atoms corresponds to a single atom type (M3 and M4 become symmetry equivalent; A1–A3 become symmetry equivalent). When superimposed, the two images show the most pronounced difference in the buckminsterfullerene-type (outermost) cage. In the cubic R-phase structures, not only are the M3 and M4 sites crystallographically inequivalent, but they also contain different elemen-

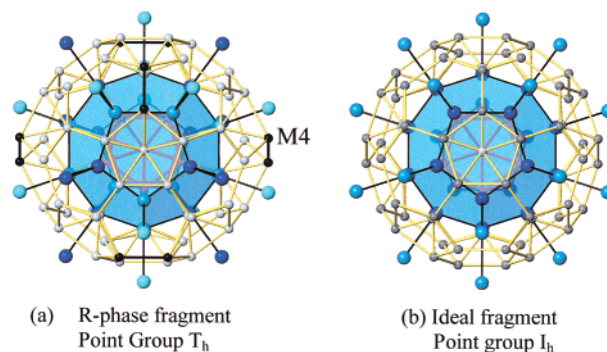


Figure 9. (a) Fragment of the R-phase structure (point group T_h) showing three shells of M sites and two shells of A sites projected down a pseudo-5-fold axis $[3^{1/2}, 1, 0]$. (b) The same fragment as in (a) with the point group I_h (the average interatomic distances were obtained from the R-phase structure).

tal compositions, which included vacancies at the M4 position. These sites prevent the formation of 5-fold symmetry that can lead to the formation of a quasicrystalline phase, and this suggests that the M4 sites may play a crucial role in the formation of quasicrystalline phases in the Mg–Zn–Al system.

Conclusions

This study reports the first detailed and systematic experimental and theoretical investigation of the crystalline R-phases in the Mg–Zn–Al system, which have been used to model quasicrystalline materials in the same ternary system. Elemental analyses coupled with X-ray and neutron diffraction experiments were necessary to elucidate the structural chemistry at the various sites in the R-phase structure. Theoretical calculations provided models to interpret some exceptional features of these materials: (1) nonbonding character of the M–M contacts exists over a range of VEC, which can account for the observed phase width; (2) two M sites (M1 and M3) are responsible for the phase width, while the other two M sites (M2 and M4) are essentially fixed in chemical composition (or in VEC); (3) the M4 site allows occupation by vacancies, Zn, and Mg atoms; and (4) vacancies arise in the structure because the VEC exceeds the value that optimizes M–M bonding. Since the vacancy concentration is linked to both VEC and the observation of quasicrystalline phases, we continue to investigate the chemistry and properties of these materials.

Acknowledgment. This work was supported by the NSF DMR 96-27161 and DMR 99-81766. The authors gratefully thank Dr. R. A. Jacobson for the use of X-ray diffractometers, Dr. Ilia Guzei for training on the Bruker CCD-1000 diffractometer (which was purchased with funds from Grant NSF 97-11121), Dr. J. Richardson at Argonne National Laboratory for neutron powder diffraction experiments, Dr. I. A. Fisher for conductivity measurements, A. W. Straszheim for EDS experiments, R. Terpstra for pycnometric measurements, and J. Ostenson for magnetic susceptibility measurements.

Supporting Information Available: Tables of crystallographic data and anisotropic displacement parameters for 1–6 and analysis of Guinier powder X-ray diffraction films for 1–3; figures showing COOP curves, magnetic susceptibility measurements, and temperature-dependent resistivity measurements; and a table of the composition of the M4 site from neutron data using different models of Mg/Zn/Al/v combinations (PDF). This material is available free of charge via the Internet at <http://pubs.acs.org>.